

# Neuromorphic Imaging with Joint Image Deblurring and Event Denoising

Pei Zhang, Haosen Liu, Zhou Ge, Chutian Wang and Edmund Y. Lam, *Fellow, IEEE*

**Abstract**—Neuromorphic imaging reacts to per-pixel brightness changes of a dynamic scene with high temporal precision and responds with asynchronous streaming events as a result. It also often supports a simultaneous output of an intensity image. Nevertheless, the raw events typically involve a great amount of noise due to the high sensitivity of the sensor, while capturing fast-moving objects at low frame rates results in blurry images. These deficiencies significantly degrade human observation and machine processing. Fortunately, the two information sources are inherently complementary — events with microsecond temporal resolution, which are triggered by the edges of objects that are recorded in latent sharp images, can supply rich motion details missing from the blurry images. In this work, we bring the two types of data together and propose a simple yet effective unifying algorithm to jointly reconstruct blur-free images and noise-robust events, where an event-regularized prior offers auxiliary motion features for blind deblurring, and image gradients serve as a reference to regulate neuromorphic noise removal. Extensive evaluations on real and synthetic samples present our superiority over other competing methods in restoration quality and greater robustness to some challenging realistic scenarios. Our solution gives impetus to the improvement of both sensing data and paves the way for highly accurate neuromorphic reasoning and analysis.

**Index Terms**—Neuromorphic Imaging, Event, Image Deblurring, Event Denoising, Information Fusion.

## I. INTRODUCTION

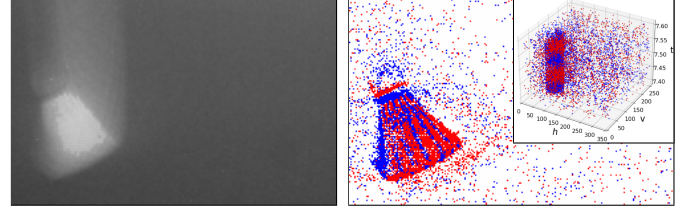
NEUROMORPHIC cameras, equipped with a dynamic vision sensor (DVS), output asynchronous events within microseconds in response to pixel-level brightness changes of a dynamic scene, such that they are competent at recording fast motion with reduced blur [1]. Some cameras that are also bundled with an active pixel sensor (APS) can capture events and intensity frames in parallel [2]. Such a bio-inspired imaging has been bringing new applications in recent years [3]–[6]. However, there are two issues that often arise in many scenarios:

- 1) The DVS reacts to dynamic objects, posing challenges to the low frame-rate APS that produces blurry images when there is a relative movement between the camera and imaging scenes during the exposure time. Although

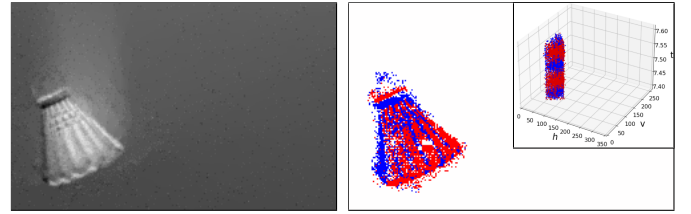
This work was supported in part by the Research Grants Council of Hong Kong SAR (GRF 17201620, 17200321) and by ACCESS — AI Chip Center for Emerging Smart Systems, sponsored by InnoHK funding, Hong Kong SAR.

The authors are with the Department of Electrical and Electronic Engineering, The University of Hong Kong, Pokfulam, Hong Kong SAR, China (e-mail: {zhangpei, hslu, gezhou, ctwang, elam}@eee.hku.hk). Edmund Y. Lam is also affiliated with ACCESS — AI Chip Center for Emerging Smart Systems, Hong Kong Science Park, Hong Kong SAR, China.

Corresponding author: Edmund Y. Lam.



(a) The APS with a low frame rate captures a blurry image for the fast-moving badminton (left), and the DVS outputs a lot of noise in the static background (right).



(b) The two reconstructions from our approach. The events with high temporal precision assist image deblurring (left), and the estimated sharp image with clear edges steers event denoising (right).

Fig. 1. A badminton in free fall. The proposed algorithm processes a blurry image and a stream of noisy (raw) events, and outputs the corresponding sharp image and denoised events. The events are shown in two-dimensional and three-dimensional views.

the DVS suffers much less from motion blur, it presents a paradigm shift against the APS in information acquisition and loses low-frequency components by which human vision identifies fine-grained things.

- 2) The DVS is susceptible to various sources of interference (e.g., sensor jitter and harsh illumination) and can return events with a lot of noise in response. Noise appears in the pixels with a lack of any active motion and substantially lowers processing accuracy.

As such, the camera typically generates blurry images and noisy event streams for highly dynamic scenes, as shown in Figure 1 (a). The issues can be rather exacerbated for low illumination conditions, in which the noise level of the DVS becomes higher [7] and the images of the APS are more blurry due to the increasing exposure time for image formation, leading to significantly degraded observations and analysis.

The key to solving these challenges is the interplay between asynchronous events and synchronous images, where the strengths of each can be leveraged to compensate for the deficiencies of the other. Events with microsecond temporal precision encode abundant motion information and can implicitly supply blind deblurring with a latent ground truth. On the other hand, while noise is irregular in space-time, informative events arise from the edges of a moving object that is clearly recorded in a sharp image, and the sharp image can thus offer

accurate priors for event denoising.

Fusing blurry images with events has delivered precise image reconstructions [8]–[11], and leveraging images as event noise filters has shown impressive results [12]. Nevertheless, existing solutions only focus on one-sided reconstructions and fail to recognize that the two kinds of data can collaborate with each other to improve restoration quality, and their processing is thus heavily affected by the other side that is suffering from anomalous states. For example, the deblurring is subject to event noise and thus requires lots of events for support [8], [9], and the denoising can be malfunctioned by blurry images [12].

In this work, we introduce a unifying processing structure for the joint restoration of the blurry images and noisy events generated by a single neuromorphic camera, to simultaneously acquire blur-free images and noise-robust events (as shown in Figure 1). Specifically, an event-regularized prior is proposed for blind image deblurring in which the events are leveraged to supply auxiliary motion features for the blurry image. The estimated sharp image can provide gradient information that steers accurate discrimination between events and noise. With an iterative fashion, the two outputs are progressively refined. Experiments are based on our dataset, which includes multiple pairs of blurry images and noisy event streams recorded by a DAVIS346 camera on challenging scenarios. Assessed on real and synthetic samples, our solution gives better results compared with competing methods.

This paper is structured as follows. Some pertinent studies are briefly reviewed in Section II. In Section III, we elucidate the proposed methods that serve joint image and event reconstruction. Section IV elaborates experiment designs and the findings compared with other approaches. The paper ends with some concluding remarks in Section V. We offer supplementary information along with a few observations of the limitation of our work in Appendix.

## II. RELATED WORK

### A. Neuromorphic Imaging

Neuromorphic cameras (or neuromorphic imaging), which have higher temporal resolution and higher dynamic range than conventional frame-based sensors, record local brightness changes in the form of sparse and asynchronous events [1]. Such outstanding features make the imaging modality innately suitable for highly dynamic scenes under extreme illumination. Nevertheless, it generates time-sequence data streams that present a paradigm shift against frame-based imaging in visual information acquisition. To handle the streaming readout, some investigations tried to design alternative event-based manifestations (*e.g.*, event frames [13] and graphs [14]), such that these new representations can inherit the advantages of events and can also be compatible with proven vision algorithms. Accordingly, a variety of event-driven solutions have been developed for downstream applications, such as optical flow estimation [15], motion prediction [3], segmentation [16] and autofocus [17]. In addition, increasing advances in processing technologies also give rise to a number of neuromorphic datasets, which are built either on simulators [18] or on real-scene capture [19].

### B. Blind Image Deblurring

Motion blur corrupts the images when there is a movement between the camera and the objects being captured. Blind image deblurring is an inverse process where we try to estimate a potential blur kernel and recover a latent sharp image [20]. There are two branches of research on image reconstruction, and one of them is the optimization only relying on a known blurry image, such as Pan *et al.* [21] who proposed a revised  $L_0$  regularization tailored for text images, Dong *et al.* [22] where an outlier-robust algorithm was developed to alleviate artifacts, and Pan *et al.* [23] in which the issue was addressed by effective image phase analysis. In addition, recent studies are more in favor of learning-based methods that can bring greater robustness and higher accuracy from a mass of learned parameters [24].

Since neuromorphic cameras can capture high-speed motion with microsecond precision, another branch tries to incorporate event features into image reconstruction, taking advantages of the two information sources. Specifically, Scheerlinck *et al.* [8] designed a novel complementary filter to bring frames into being a greater temporal resolution and dynamic range state. Pan *et al.* [9], [25] probed into an event-based double integral model to fuse blurry frames with the associated events and achieved impressive restoration. Wang *et al.* [10] leveraged a kind of event-oriented augmentation whereby frames are enhanced with deblurring and temporal interpolation. Similarly, data-driven approaches are also transferred to the neuromorphic field and proved to acquire convincing results [11], [26].

### C. Neuromorphic Noise Removal

Sensitive neuromorphic cameras are highly vulnerable to various types of interference and can output noise as a result. This work is concerned with Background Activity (BA) noise. In bright scenes, the noise mainly results from junction leakage currents, while it is caused by thermal noise in dark scenes [6]. Besides, due to threshold mismatch issues, the cameras also have hot-pixels in which the noise is fired at an abnormally high rate at the same positions [18]. In relative to the noise behaving irregularly in space-time, events triggered by the edges of moving objects typically have strong continuity and correlation [27].

There have already been pioneering studies that achieved early progress on noise removal. Nearest neighbor-based filters built on local spatiotemporal correlation were first developed to suppress BA noise [28], and subsequent research presented substantial enhancements in memory optimization [29]. Offline approaches are being intensively studied due to their computing capacity and scalability, albeit they are potentially inappropriate for in-camera operations due to non-deterministic runtime. For example, event density [27], [30], which suggests that events typically shape a denser cluster, and event probability [31], where the denoising is modelled as an energy minimization process, can discriminate between events and noise. As artificial intelligence evolves, recent research also made use of deep neural networks to learn patterns on massive raw events for noise suppression [32], [33].

### III. METHODOLOGY

#### A. Neuromorphic Imaging Preliminary

Once a logarithmic photocurrent change at a spatial position  $\mathbf{x}$  exceeds a specific threshold at time  $t$ , neuromorphic cameras generate and encode an event  $\mathbf{e}$ , denoted by

$$\mathbf{e}_i = (\mathbf{x}, t_i, p_i), \quad (1)$$

where  $i$  indexes the event at a pixel  $\mathbf{x} = (h, v)^\top$  consisting of two orthogonal directions  $h$  and  $v$ . The symbol  $p_i \in \{-1, +1\}$  indicates the sign of the photocurrent change. Since the time  $t$  varies continuously, an event can also be modelled as

$$\mathcal{M}(\mathbf{e}_i) = \tilde{\mathbf{e}}_i(t) = p_i \delta(t - t_i), \quad (2)$$

where  $\delta(t)$  is the Dirac delta function<sup>1</sup>, and  $\mathcal{M}$  is a mapping from a spatiotemporal node to a pixel in an image. Since the function  $\tilde{\mathbf{e}}_i(t)$  applies to every coordinate, we omit  $\mathbf{x}$  in the above expression. Similarly, we define  $\mathbf{E}$  for a batch of events

$$\mathbf{E} = \{\mathbf{e}_i\}_{i=1:\infty} = \{(\mathbf{x}, t_i, p_i)\}_{i=1:\infty}. \quad (3)$$

We then transform a discrete event stream  $\mathbf{E}$  into a continuous-time signal  $\mathcal{M}(\mathbf{E}) = \tilde{\mathbf{E}}(t)$  that incorporates a sequence of impulses

$$\tilde{\mathbf{E}}(t) = \sum_{i=1}^{\infty} \tilde{\mathbf{e}}_i(t) = \sum_{i=1}^{\infty} p_i \delta(t - t_i). \quad (4)$$

We integrate  $\tilde{\mathbf{E}}(t)$  over a time interval to obtain the approximate intensity (change)  $\mathbf{I}_\tau(t)$

$$\mathbf{I}_\tau(t) = \int_{t-\tau}^t \tilde{\mathbf{E}}(\zeta) d\zeta = \int_{t-\tau}^t \sum_{i=1}^{\infty} p_i \delta(\zeta - t_i) d\zeta, \quad (5)$$

where a set of events within the time window  $\tau$  are integrated. The intensity increment for a short period  $\Delta t$  is defined as

$$\Delta \mathbf{I}_\tau(t) = \mathbf{I}_\tau(t) - \mathbf{I}_\tau(t - \Delta t), \quad (6)$$

which can be approximated by

$$\Delta \mathbf{I}_\tau(t) \approx \frac{\partial}{\partial t} \mathbf{I}_\tau(t) \Delta t. \quad (7)$$

Based on the brightness constancy assumption for any short period  $\Delta t$  [34], we have

$$\frac{\partial}{\partial t} \mathbf{I}_\tau(t) + \nabla_{\mathbf{x}} \mathbf{I}_\tau(t) \cdot \mathbf{v} = 0, \quad (8)$$

where  $\nabla_{\mathbf{x}} = (\partial_h, \partial_v)^\top$  symbolizes the differential operator,  $\nabla_{\mathbf{x}} \mathbf{I}_\tau(t) = (\partial_h \mathbf{I}_\tau(t), \partial_v \mathbf{I}_\tau(t))^\top$  is the spatial gradient, and  $\mathbf{v} = (\frac{d}{dt} h, \frac{d}{dt} v)^\top$  denotes the motion field. We combine Equations (7) and (8) for a dot-product expression

$$\Delta \mathbf{I}_\tau(t) \approx -\nabla_{\mathbf{x}} \mathbf{I}_\tau(t) \cdot \mathbf{v} \Delta t, \quad (9)$$

showing that events arise from the edges of an imaging object moving over a distance  $\mathbf{v} \Delta t$ . The above equations theoretically corroborate image-event interconnection.

<sup>1</sup>In the following, we will alternatively use Equation (1) and Equation (2) to describe an event.

#### B. Joint Neuromorphic Reconstruction

We formulate a blurry image  $\mathbf{B}$  as the result of a convolution of a latent sharp image  $\mathbf{S}$  with a spatially invariant kernel  $\mathbf{k}$

$$\mathbf{B} = \mathbf{S} * \mathbf{k} + r, \quad (10)$$

where  $r$  is the residual, and  $*$  denotes the convolution operator. Blind image deblurring, which requires the simultaneous reconstruction of both  $\mathbf{S}$  and  $\mathbf{k}$  from available  $\mathbf{B}$ , is highly under-determined, since the same  $\mathbf{B}$  can result from different pairs of  $\mathbf{S}$  and  $\mathbf{k}$ . To achieve accurate restoration, the deblurring process can be modelled as

$$\min_{\mathbf{S}, \mathbf{k}} \|\mathbf{S} * \mathbf{k} - \mathbf{B}\|_2^2 + \mathcal{R}_{\mathbf{S}}(\mathbf{S}) + \mathcal{R}_{\mathbf{k}}(\mathbf{k}), \quad (11)$$

where the data-fidelity term expects the smallest difference between the estimated blurry image  $\mathbf{S} * \mathbf{k}$  and the observation  $\mathbf{B}$ . Two regularizers  $\mathcal{R}_{\mathbf{S}}$  and  $\mathcal{R}_{\mathbf{k}}$  constrain  $\mathbf{S}$  and  $\mathbf{k}$ , respectively. With multiple iterations, we alternatively estimate  $\mathbf{S}$  by solving

$$\min_{\mathbf{S}} \|\mathbf{S} * \mathbf{k} - \mathbf{B}\|_2^2 + \mathcal{R}_{\mathbf{S}}(\mathbf{S}), \quad (12)$$

and  $\mathbf{k}$  via

$$\min_{\mathbf{k}} \|\mathbf{S} * \mathbf{k} - \mathbf{B}\|_2^2 + \mathcal{R}_{\mathbf{k}}(\mathbf{k}). \quad (13)$$

By such iterative alternating optimization,  $\mathbf{S}$  and  $\mathbf{k}$  can be progressively refined in each update.

Since events can precisely record motion with microsecond precision, they serve as a ground truth of the gradient space for estimating  $\mathbf{S}$ . In other words, events can be a prior to shape a sharp image in which the recorded object edges triggered the existing events. We thus introduce an event-based regularizer for estimating  $\mathbf{S}$ , with

$$\mathcal{R}_{\mathbf{S}}(\mathbf{S}) = \alpha \|\nabla_{\mathbf{x}} \mathbf{S} - \mathbf{I}_\tau(t)\|_2^2 + \beta \|\nabla_{\mathbf{x}} \mathbf{S}\|_0, \quad (14)$$

where  $\alpha$  and  $\beta$  are penalty parameters. The first term imposes the spatial gradient of the reconstruction to be close to the events triggered by a latent sharp image. We also leverage an  $L_0$  gradient prior [35] as the second constraint to suppress the artifacts caused by the noise of  $\mathbf{I}_\tau(t)$  shaped by raw noisy events. In other words, we expect that the pixels of  $\nabla_{\mathbf{x}} \mathbf{S}$ , except for those on edges, do not have non-zero values. Then, we rewrite the objective function as

$$\min_{\mathbf{S}} \|\mathbf{S} * \mathbf{k} - \mathbf{B}\|_2^2 + \alpha \|\nabla_{\mathbf{x}} \mathbf{S} - \mathbf{I}_\tau(t)\|_2^2 + \beta \|\nabla_{\mathbf{x}} \mathbf{S}\|_0. \quad (15)$$

We handle the computationally intractable  $L_0$ -regularized term as earlier approaches [21], [35], [36], where Equation (15) is approximated by

$$\min_{\mathbf{S}, \mathbf{z}} \|\mathbf{S} * \mathbf{k} - \mathbf{B}\|_2^2 + \alpha \|\nabla_{\mathbf{x}} \mathbf{S} - \mathbf{I}_\tau(t)\|_2^2 + \gamma \|\nabla_{\mathbf{x}} \mathbf{S} - \mathbf{z}\|_2^2 + \beta \|\mathbf{z}\|_0, \quad (16)$$

where  $\mathbf{z} = (z_h, z_v)^\top$  is an auxiliary variable associated with  $\nabla_{\mathbf{x}} \mathbf{S} = (\partial_h \mathbf{S}, \partial_v \mathbf{S})^\top$ , and  $\gamma$  is a penalty weight. Likewise, this equation can be solved by alternating between evaluating  $\mathbf{S}$  through

$$\min_{\mathbf{S}} \|\mathbf{S} * \mathbf{k} - \mathbf{B}\|_2^2 + \alpha \|\nabla_{\mathbf{x}} \mathbf{S} - \mathbf{I}_\tau(t)\|_2^2 + \gamma \|\nabla_{\mathbf{x}} \mathbf{S} - \mathbf{z}\|_2^2, \quad (17)$$

and  $\mathbf{z}$  via

$$\min_{\mathbf{z}} \gamma \|\nabla_{\mathbf{x}} \mathbf{S} - \mathbf{z}\|_2^2 + \beta \|\mathbf{z}\|_0. \quad (18)$$

**Algorithm 1:** Joint Reconstruction of the Blur-free Image and Noise-robust Events

---

**Input :**  $\mathbf{B}, \dot{\mathbf{E}}$   
**Output:**  $\mathbf{S}, \dot{\mathbf{E}}$

- 1 Initialize  $l = 0$ , and  $\mathbf{k}^{(l)}$  from the coarser level. //  $l$  indexes iterations
- 2 Initialize  $\mathbf{I}_\tau(t)$  from  $\dot{\mathbf{E}}$  by Equations (4) and (5).
- 3 Let  $\mathbf{S}^{(l-1)} = \mathbf{B}$ , and  $\dot{\mathbf{E}} = \emptyset$ .
- 4 **while**  $l \leq l_{max}$  **do** //  $l_{max}$  defines the maximum iteration
- 5      $\gamma = 2\beta$ .
- 6     **while**  $\gamma \leq \gamma_{max}$  **do** //  $\gamma_{max}$  limits the update of  $\mathbf{S}$
- 7         With  $\gamma, \beta$ , update  $\mathbf{z}^{(l)}$  by Equation (21).
- 8         With  $\mathbf{k}^{(l)}, \mathbf{z}^{(l)}, \mathbf{I}_\tau(t)$ , update  $\mathbf{S}^{(l)}$  by Equation (19).
- 9          $\gamma = 2\gamma$ .
- 10     **end**
- 11     With  $\mathbf{S}^{(l)}$ , update  $\mathbf{g}^{(l)}$  by Equation (25).
- 12      $\dot{\mathbf{E}}(t) = \frac{\partial}{\partial t} \mathbf{I}_\tau(t)$ .
- 13     Search  $\mathbf{G}_{\mu, \nu}^{(i)}$  of  $\mathbf{e}_i \in \{\mathbf{e} \in \mathbf{E} \mid \mathbf{x} \in \mathbf{g}^{(l)} \circ \tilde{\mathbf{E}}(t)\}$  by Equation (26). // can be any search method
- 14     Evaluate  $\dot{\mathbf{E}} = \dot{\mathbf{E}} \cup \{\mathbf{G}_{\mu, \nu}^{(i)} \cup \{\mathbf{e}_i\}\}$ .
- 15     With  $\mathbf{S}^{(l)}$ , update  $\mathbf{k}^{(l+1)}$  by Equation (23).
- 16      $l = l + 1$ .
- 17 **end**

---

Given the fixed  $\mathbf{k}$  and  $\mathbf{z}$ , solving Equation (17) is a quadratic problem where the closed-form solution can be found by the Fast Fourier Transform (FFT)

$$\mathbf{S} = \mathcal{F}^{-1} \left( \frac{\overline{\mathcal{F}}(\mathbf{k})\mathcal{F}(\mathbf{B}) + \alpha \overline{\mathcal{F}}(\nabla_{\mathbf{x}})\mathcal{F}(\mathbf{I}_\tau(t)) + \gamma \hat{\mathcal{F}}(z_h, z_v)}{\overline{\mathcal{F}}(\mathbf{k})\mathcal{F}(\mathbf{k}) + (\alpha + \gamma)\hat{\mathcal{F}}(\partial_h, \partial_v)} \right), \quad (19)$$

where  $\mathcal{F}, \mathcal{F}^{-1}$  and  $\overline{\mathcal{F}}$  denote the FFT, inverse FFT and complex conjugate operator, respectively. The expression  $\hat{\mathcal{F}}(\theta_0, \theta_1)$  with two arguments  $\theta_0$  and  $\theta_1$  is defined as

$$\hat{\mathcal{F}}(\theta_0, \theta_1) = \overline{\mathcal{F}}(\partial_h)\mathcal{F}(\theta_0) + \overline{\mathcal{F}}(\partial_v)\mathcal{F}(\theta_1). \quad (20)$$

Given  $\mathbf{S}$ , Equation (18) turns into element-wise minimization with hard thresholding [35]

$$\mathbf{z} = \begin{cases} 0, & |\nabla_{\mathbf{x}}\mathbf{S}|^2 \leq \beta\gamma^{-1} \\ \nabla_{\mathbf{x}}\mathbf{S}, & \text{otherwise} \end{cases}. \quad (21)$$

Some research argues the estimation of  $\mathbf{k}$  in the gradient domain to be superior with regard to accuracy [37]. As such, with  $\mathbf{S}$  known,  $\mathbf{k}$  of Equation (13) can be updated by solving

$$\min_{\mathbf{k}} \|\nabla_{\mathbf{x}}\mathbf{S} * \mathbf{k} - \nabla_{\mathbf{x}}\mathbf{B}\|_2^2 + \sigma \|\mathbf{k}\|_2^2, \quad (22)$$

where  $\sigma$  is a weight for the Gaussian regularizer  $\mathcal{R}_{\mathbf{k}}(\mathbf{k}) = \|\mathbf{k}\|_2^2$ . Similarly, this minimization can be solved by the FFT

$$\mathbf{k} = \mathcal{F}^{-1} \left( \frac{\overline{\mathcal{F}}(\nabla_{\mathbf{x}}\mathbf{S})\mathcal{F}(\nabla_{\mathbf{x}}\mathbf{B})}{\overline{\mathcal{F}}(\nabla_{\mathbf{x}}\mathbf{S})\mathcal{F}(\nabla_{\mathbf{x}}\mathbf{S}) + \sigma} \right). \quad (23)$$

We then set the negative elements of  $\mathbf{k}$  to 0 and normalize  $\mathbf{k}$ .

Streaming events are triggered by moving edges, whereas BA noise is randomly distributed throughout the static background. Equation (19) gives a recovered sharp image  $\mathbf{S}$  that can provide accurate edge information. With the support of

the given gradient prior  $\nabla_{\mathbf{x}}\mathbf{S}$ , we steer neuromorphic noise removal and define the denoised events  $\dot{\mathbf{E}}$  as

$$\dot{\mathbf{E}} = \mathcal{M}^{-1} \left( \mathbf{g} \circ \tilde{\mathbf{E}}(t) \right), \quad (24)$$

where  $\mathcal{M}^{-1}$  is the inverse function of  $\mathcal{M}$  to retrieve a space-time node from the pixels a mask  $\mathbf{g}$  shares with the raw events  $\tilde{\mathbf{E}}(t)$ . The symbol  $\circ$  denotes element-wise multiplication. The element  $\mathbf{g}_i$  of  $\mathbf{g}$  simply follows

$$\mathbf{g}_i = \begin{cases} 0, & \nabla_{\mathbf{x}}\mathbf{S}_i \in (c - \omega, c + \omega) \\ \nabla_{\mathbf{x}}\mathbf{S}_i, & \text{otherwise} \end{cases}, \quad (25)$$

where  $\omega$  is a calibration factor,  $c$  is the pixel value of  $\nabla_{\mathbf{x}}\mathbf{S}$  with the most occurrences, and  $\nabla_{\mathbf{x}}\mathbf{S}_i$  is an element of  $\nabla_{\mathbf{x}}\mathbf{S}$ . Combining Equations (24) and (25), we can couple events with the spatial gradient of a sharp image.

To prevent the events triggered by large motion that cannot be sufficiently represented by image edges from being filtered out, we exploit the spatiotemporal correlation principle — events tend to be temporally correlated with their spatial neighbors [29], which can be mathematically expressed as

$$\mathbf{G}_{\mu, \nu}^{(i)} = \{\mathbf{e}_j \in \mathbf{E} \mid \mathcal{D}_{\mathbf{x}}(\mathbf{e}_j, \mathbf{e}_i) \leq \mu, \mathcal{D}_t(\mathbf{e}_j, \mathbf{e}_i) \leq \nu\}, \quad (26)$$

where an event  $\mathbf{e}_j$  is regarded as one of the spatiotemporal neighbors  $\mathbf{G}_{\mu, \nu}^{(i)} \in \mathbf{G}_{\mu, \nu}$  of an event  $\mathbf{e}_i$  if the two events are sufficiently near in space-time. The functions  $\mathcal{D}_{\mathbf{x}}, \mathcal{D}_t$  evaluate the spatial and temporal distance respectively, and  $\mu, \nu$  are case-dependent thresholds. Equation (24) can thus be rewritten as

$$\dot{\mathbf{E}} = \mathcal{M}^{-1} \left( \mathbf{g} \circ \tilde{\mathbf{E}}(t) \right) + \mathbf{G}_{\mu, \nu}, \quad (27)$$

indicating that the expected signal should comprise the events at the image edges and their space-time neighbors.

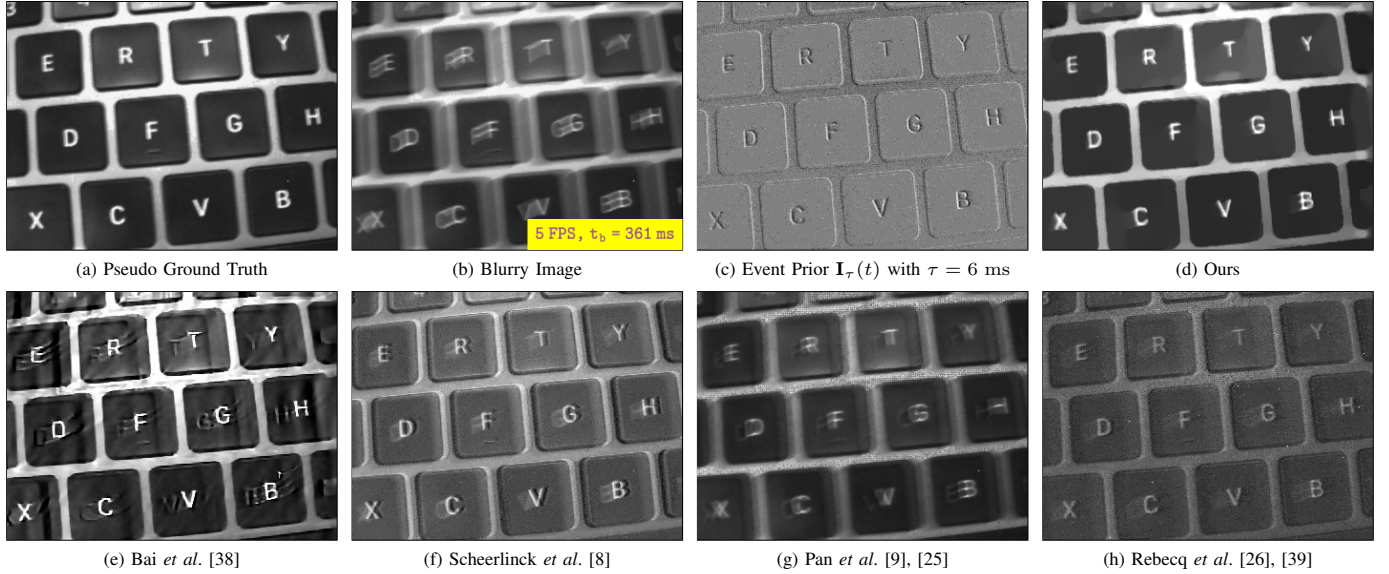


Fig. 2. Visual comparisons on deblurring the image with uniform motion blur. (a) A sharp image at a certain timestamp serves as a ground truth for reference. (b) The blurry image to be processed. (c) The used event prior. (d) Our reconstruction has more faithful shapes and shades of gray. (e) The image-based method has distortions and ringing artifacts in some pixels. (f)–(h) The results of the competing event-based approaches, where (f) leaves blur residues and (g), (h) involve a mass of gray flecks.

Algorithm 1 shows a dedicated workflow to bridge the two imaging modalities for joint reconstruction of the blur-free image and noise-robust events. The iterative processing enables coarse-to-fine reevaluations of  $\mathbf{S}$  and  $\dot{\mathbf{E}}$ , while attenuating the noise effect from raw events (*i.e.*, Line 2 of Algorithm 1) on  $\mathbf{S}$  is realized by  $\beta$  of Equation (15), where we penalize the pixels that are not on edges, and the one on  $\dot{\mathbf{E}}$  is accomplished by  $\omega$  of Equation (25), by which we filter the events in less active pixels.

We have an **assumption** that there is always a latent sharp image in which the recorded objects can be captured by events. Given the timestamp  $t_b$  of a blurry image we are processing, the  $\tau$  of the event prior  $\mathbf{I}_\tau(t)$  has  $t_b = t - \frac{\tau}{2}$ . That is, the sharp image at  $t_b$  is blurred during the exposure time  $[t_b - \frac{\tau}{2}, t_b + \frac{\tau}{2}]$ .

#### IV. EXPERIMENTS

##### A. Blurry Images and Noisy Events Dataset

We collect a real neuromorphic dataset made up of multiple pairs of blurry images and noisy events to evaluate our approach and other counterparts. The neuromorphic camera DAVIS346 [2], with a spatial resolution of  $346 \times 260$  pixels and a 120 dB DVS dynamic range, is used to capture images and events in parallel from real dynamic scenes. We first record objects with the static camera for obtaining blur-free references, and then shake the camera during imaging such that the images suffer from uniform motion blur. After similar preparations for static image recordings, we also film objects moving at a high speed against a static background and thus acquire the results with non-uniform blur. To make images underexposed or overexposed, targets are placed under low or strong illumination. Incandescent lighting with 60 Hz serves as the source, and there is BA noise in raw events accordingly. This dataset also applies to the evaluation of traditional image

reconstruction algorithms or pure event denoising approaches. More details are given in Appendix A.

##### B. Evaluations on Blind Image Deblurring

Our solution and several state-of-the-art counterparts are assessed on sharpening the image with uniform blur in Figure 2 and the one with non-uniform blur in Figure 3. In both experiments, the clear images of a scene are captured and serve as pseudo ground truth, becoming a reference for the structures and shapes of the imaging scene to visually evaluate the reconstructions of a real blurry image.

When recovering the sharp state of the blurry image with uniform motion, the image-based method, Figure 2 (e), suffers from serious ringing artifacts, whereas the event-based ones, Figure 2 (f)–(h), have better reconstructions in comparison. However, they either leave blurry residues or contain noticeable gray flecks (caused by event noise). With the precise motion capture as a prior, our algorithm shapes a clearer image and visually outperforms all the competing counterparts by large margins.

It becomes much more challenging to find the sharp shape of a non-uniform blurry image where imaging objects are moving against static scenes, such that there is inconsistent blur in the foreground and background. Our uniform deblurring method can be extended to non-uniform blur processing, and the explanations are given in Appendix B. Figure 3 (b) highlights two positions with different blur states, and only one of them has a significant movement as Figure 3 (c) reveals. Compared with the image-based method, the event-based ones obtain clearer reconstructions since events can precisely locate active pixels, and ours gives sharper texts and brings fewer artifacts on the pixels of the dynamic foreground.

Quantitative evaluations are conducted based on the DAVIS 240C Datasets [40], where we leverage the Mean Squared



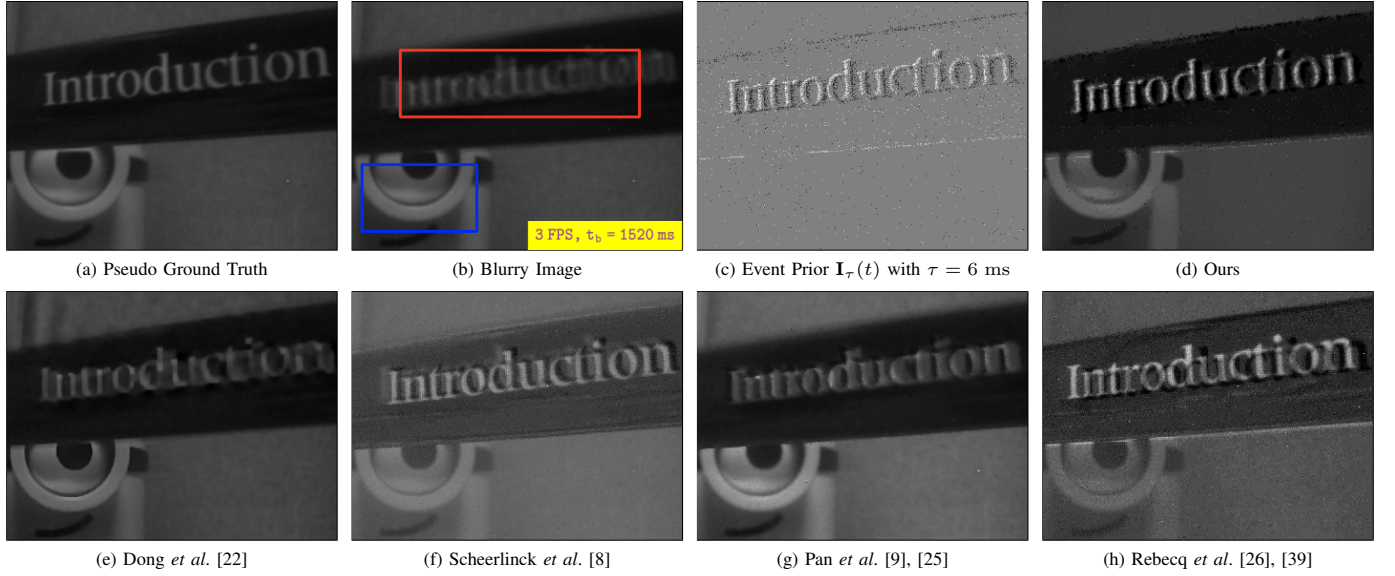


Fig. 3. Visual comparisons on deblurring the image with non-uniform motion blur. (a) A sharp image at a certain timestamp serves as a ground truth for reference. (b) The raw image, where the blurry foreground to be processed is highlighted with a red box, and the static background is marked by a blue box. (c) The used event prior. (d) Our image has clearer visualization of the deblurred texts. (e) The image-based algorithm still leaves severe blur residues. (f)–(h) The reconstructions of the competing event-based methods present different degrees of artifacts caused by the offset of the events from the raw image.

TABLE I  
QUANTITATIVE COMPARISONS ON BLIND IMAGE DEBLURRING.

Type	Algorithm	Evaluation		
		MSE ↓	LPIPS ↓	SSIM ↑
Image	Synthetic Blur	5.34	22.52	0.17
	Dong <i>et al.</i> [22]	3.59	12.62	0.28
	Bai <i>et al.</i> [38]	4.05	13.05	0.25
	Chen <i>et al.</i> [37]	3.34	15.22	0.35
	Pan <i>et al.</i> [23]	3.67	12.87	0.32
	<b>Ours</b>	<b>1.95</b>	<b>5.72</b>	<b>0.47</b>
Event	Scheerlinck <i>et al.</i> [8]	3.04	10.14	0.39
	Pan <i>et al.</i> [9], [25]	2.87	9.26	0.35
	Rebecq <i>et al.</i> [26], [39]	2.98	6.53	0.41
	Wang <i>et al.</i> [10]	3.22	7.79	0.39
	<b>Ours</b>	<b>1.95</b>	<b>5.72</b>	<b>0.47</b>

Error (MSE) to measure the difference in pixels, Perceptual Loss (LPIPS with scaling) to evaluate the variation in deep features [41] and Structural Similarity Index Measure (SSIM) to assess the resemblance in structural details. An effective algorithm is expected to earn a low value of MSE, LPIPS, and a high value of SSIM. Table I presents that our solution delivers the best results in all the metrics, indicating that our reconstructions and the original data have few changes in pixel values, deep features and structural information. Specifically, compared with the event-based counterparts, ours has nearly 50% of the LPIPS of Scheerlinck *et al.*'s and surpasses the SSIM of Pan *et al.*'s by over 0.1.

### C. Event-based Reconstructions for Challenging Scenarios

Events feature high temporal precision and high dynamic range, enabling clear recordings of fast-motion and the details almost missing from underexposed or overexposed images.

TABLE II  
QUANTITATIVE COMPARISONS ON NEUROMORPHIC NOISE REMOVAL.

Sample	Algorithm	Evaluation			
		TPR	FPR	PPV	ACC ↑
Running	NN-Filter [42]	0.56	0.49	0.70	0.54
	Feng <i>et al.</i> [30]	0.59	0.19	0.86	0.66
	Wu <i>et al.</i> [31]	0.64	0.39	0.77	0.63
	EDnCNN [32]	0.73	0.46	0.76	0.66
	<b>Ours</b>	<b>0.76</b>	<b>0.30</b>	<b>0.84</b>	<b>0.74</b>
	<b>Ours</b>	<b>0.76</b>	<b>0.30</b>	<b>0.84</b>	<b>0.74</b>
Shapes	NN-Filter [42]	0.84	0.29	0.85	0.80
	Feng <i>et al.</i> [30]	0.82	0.04	0.97	0.86
	Wu <i>et al.</i> [31]	0.85	0.26	0.87	0.81
	EDnCNN [32]	0.90	0.27	0.87	0.84
	<b>Ours</b>	<b>0.93</b>	<b>0.20</b>	<b>0.90</b>	<b>0.89</b>
	<b>Ours</b>	<b>0.93</b>	<b>0.20</b>	<b>0.90</b>	<b>0.89</b>

Figure 4 shows four challenging scenarios — a text object captured by a shaking camera under low illumination in which the blurry, underexposed image almost loses dark contents; a low-lighting pedestrian scene where the raw image is severely blurry, delayed and overexposed in some pixels due to a large period of exposure time necessary for image formation [8]; recording a box with letters on it under strong illumination, which causes the overexposed image to lose shapes and textures; shooting a high-speed badminton under sufficient lighting where the image still undergoes heavy motion blur. Since the raw images have incomplete information, image-based methods cannot function properly to give reasonable reconstructions. The comparisons, where all the approaches are supported by the same number of events, show that our images have more recovered details and look more realistic.



Fig. 4. Reconstructing the images captured in challenging scenes. (a) The raw images suffer from information loss due to the nature of the APS. (b) Our results, which are based on around 14 000 (collected in 2 ms), 3 000 (4 ms), 28 000 (10 ms) and 11 000 (20 ms) events respectively, have clearer shapes and more delicate textures. (c)–(d) The results of the state-of-the-art event-based methods, whose shades of gray and textures are less faithful to the original.

#### D. Evaluations on Neuromorphic Noise Removal

The DVS is vulnerable when illumination is not constant and can accordingly respond with a great amount of BA noise. Figure 5 shows the comparisons on neuromorphic noise removal, and (a) spotlights the challenging regions containing both events and noise. Whereas the competitors either fail to suppress noise or erase lots of informative events, our method has more accurate discrimination.

Quantitative denoising analysis is performed on the samples `outdoors_running` (Running), `shapes_rotation` (Shapes) of the DAVIS 240C Datasets [40], where each sample has synthetic random noise with the amount of 50% of the number of the raw events. Instead of conducting evaluations on the Signal-to-Noise Ratio that is biased when the aggressive denoising achieves a high score by removing noise along with a significant number of true events, we consider the denoising as a binary classification task, in which a filter classifies an event as signal (positive class) or noise (negative class). The statistics — the True Positive Rate (TPR), False Positive Rate

(FPR), Precision (PPV) and Accuracy (ACC), are measures of the classifier performance.

Table II presents the comparisons, and the Nearest Neighbor Filter (NN-Filter) — the prototype accepting the events with strong spatiotemporal correlation [42], acts as a baseline. Our approach correctly classifies signal and achieves the highest TPR, and then obtains the second best FPR and PPV behind Feng *et al.*'s. However, combining the low value of TPR of Feng *et al.*'s, we infer that it has good noise removal but also discards lots of true events. As such, neither one of TPR, FPR and PPV alone can sufficiently represent the performance. The ACC measures how accurate a method is to classify both signal and noise. Our algorithm acquires the highest ACC and thus features better denoising capabilities over the counterparts.

#### E. Denoising for Fast- and Slow-moving Objects

Actively moving objects can trigger lots of events, whereas the denoising becomes more challenging when objects hardly move, such that the events have weaker spatiotemporal cor-

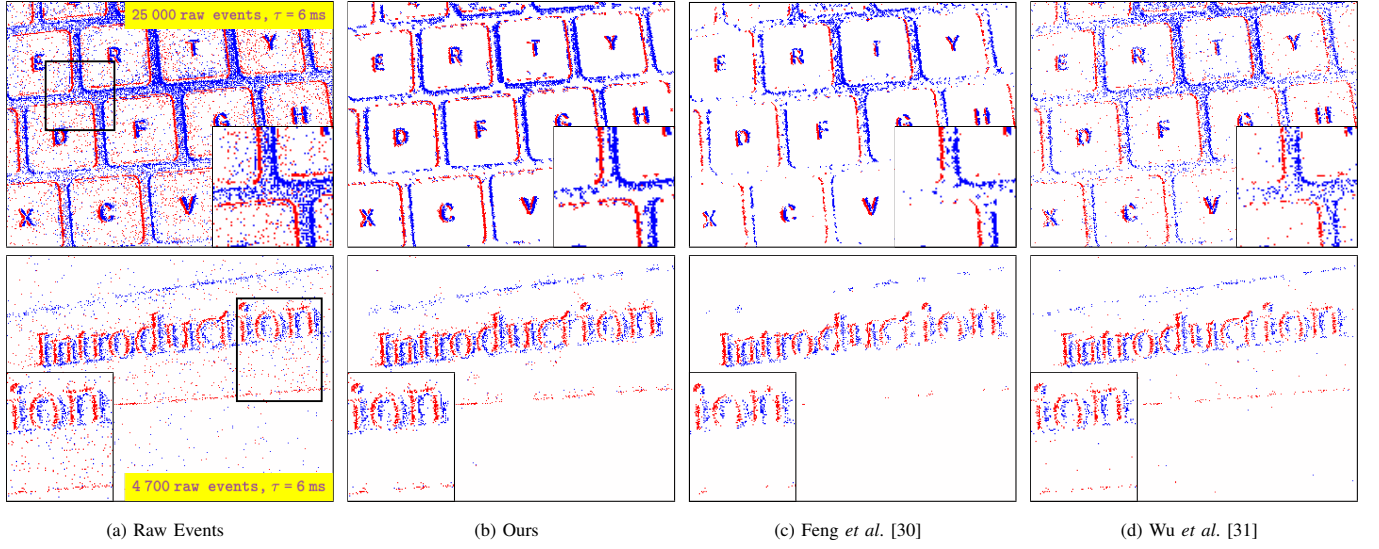


Fig. 5. Noise removal of the raw events triggered by the objects of Figures 2 and 3. We use two-dimensional event frames to visualize the event streams. (a) Raw noisy data, where the marked zones with zoom-in consist of events and noise. (b) Our results, where we suppress most of noise and faithfully retain events. (c)–(d) The results of the counterparts, where (c) loses a significant number of events, and (d) keeps events as well as a small amount of sparse noise.

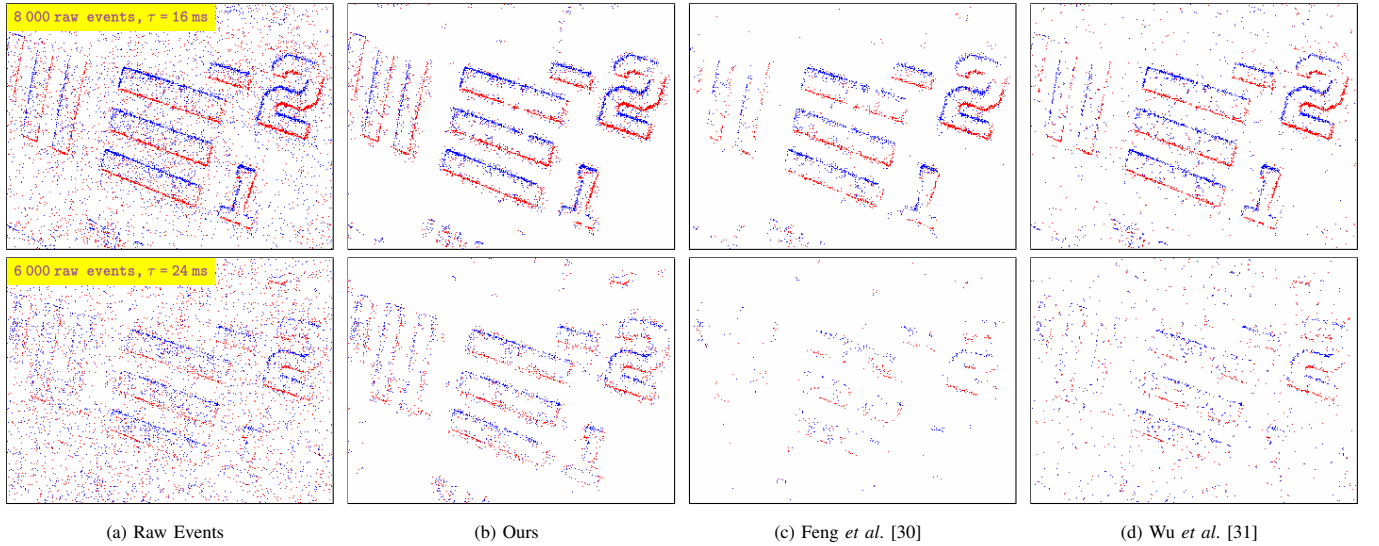


Fig. 6. Noise removal of the raw events from a fast-moving object (1st row) and a slow-moving object (2nd row). (a) Raw noisy data. The events of the fast-moving object are much denser but as sparse as noise when the object barely moves. (b) Our results have considerably reduced noise and faithfully retained events. (c) For the slow-moving case, the density-based mechanism mistakes events for sparse noise since there is no significant difference in density. (d) The results still have observable noise in the background.

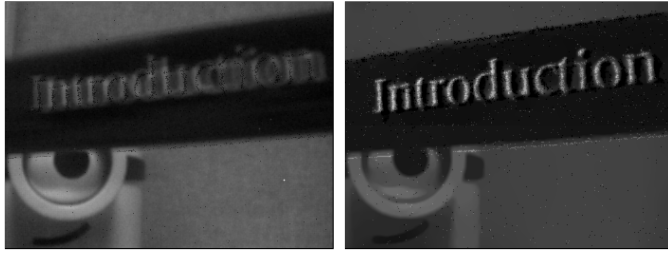
relation and account for a lower proportion in number. We study the reactions of existing algorithms to these two cases in Figure 6. In the raw data, we can visually distinguish events and noise for the fast-moving object based on pixel density but fail in the slow-moving one. All the examined methods achieve comparable results in the first case, whereas when no configuration changes of each one for the slow-moving scenario, the counterparts either leave visible noise residues or barely retain events. By comparison, our gradient-driven mechanism is less sensitive to such variations in event attributes and distribution, and features more reliable processing for the cases with a sharp drop in the number of events.

#### F. Analysis of Event Number for Image Deblurring

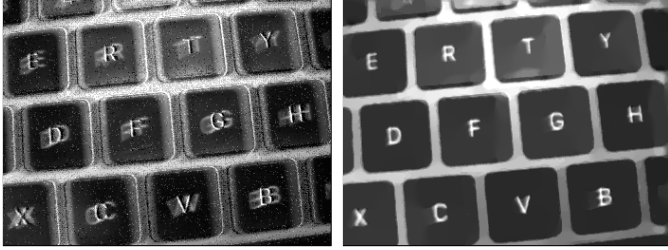
The number of events utilized for supporting the deblurring dominates the quality of reconstructed images. While increasing the quantity supplies richer dynamic features and typically leads to better results, it also causes more processing latency. As such, we expect good restoration built upon the supplemental information given by a small number of events. In Figure 7 (a) and (b), we compare ours with state-of-the-art solutions by visually evaluating the deblurred images that are based on varying numbers of events. Our method can recover clear images with the support of very few events, whereas the counterparts still leave severe motion blur.

Figure 7 (c) gives quantitative analysis on synthetic samples.

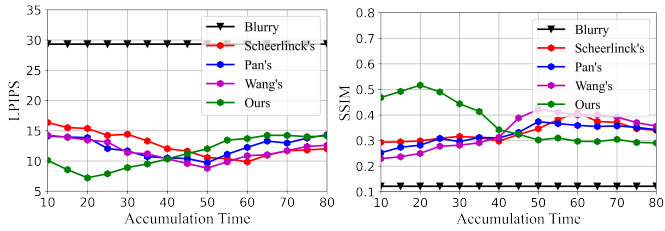




(a) The results of Pan *et al.* [9], [25] (left) and ours (right) based on 4 700 events.



(b) The results of Scheerlinck *et al.* [8] (left) and ours (right) based on 25 000 events.



(c) LPIPS and SSIM achieved when using the events accumulated over an increasing time period (in milliseconds).

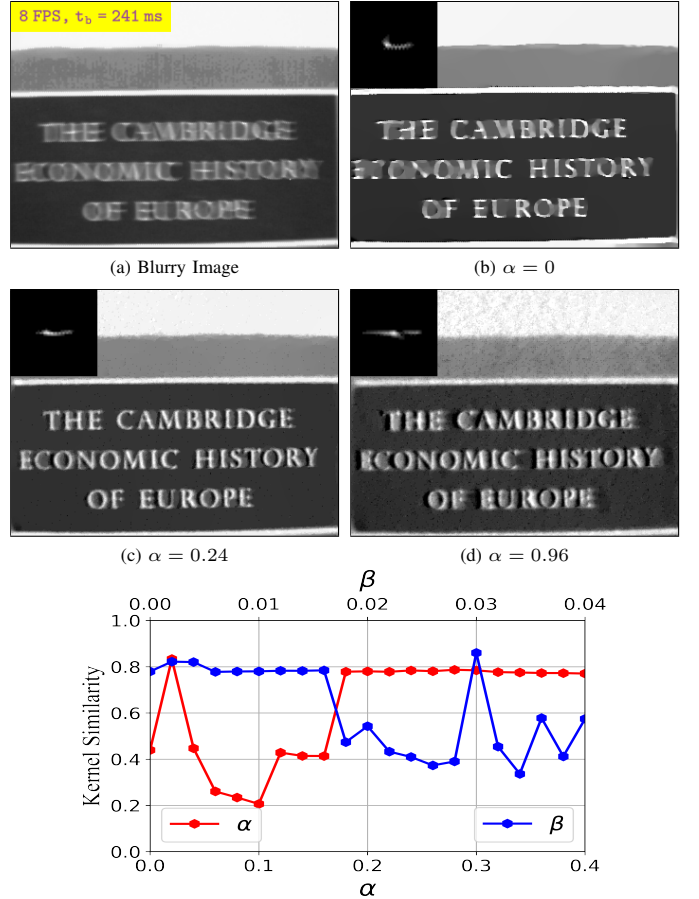
Fig. 7. Visual and quantitative results of the competing methods and ours when exploiting different numbers of events to be complementary information.

Our method achieves much more outstanding scores based on a small number of events collected within 40 ms. We note that our performance degrades with the increase of the event accumulation time. A potential reason could be that as using excessive events, our mechanism performs poorly since the batch of events covers multiple scenes whose redundant information is irrelevant to the latent sharp state. Similar issues can also be found in the competing methods, and the optimum of each relates to how the events are represented in processing. The above evaluations show that our approach can be driven by much fewer events and has higher event utilization efficiency, which is preferable when available resources are limited.

#### G. Analysis of the Regularizers for Deblurring

As in Equation (15), the deblurring operation is constrained by an event-based regularizer and an  $L_0$  term. Figure 8 analyzes how the weight  $\alpha$ , with a properly fixed  $\beta$ , affects the processed images. When  $\alpha = 0$ , and the  $L_0$  term becomes the only constraint, the blurry image is deficiently sharpened and slightly smoothed, indicating that the  $L_0$  facilitates smoothness (or noise suppression) in our cases. Increasing the value of  $\alpha$  enforces the image to approach the coarse event intensity in shades of gray and shapes, and to involve more artifacts resulting from event noise accordingly. The effects of the  $L_0$  regularization are shown in Appendix C.

Figure 8 (e) provides measurable evaluations of how the constraints impact blur kernel estimation, and higher similarity



(e) Effects of the used regularizers on kernel similarity.

Fig. 8. (a)–(d) Impacts of  $\alpha$  (when  $\beta = 0.064$ ) on image deblurring. When  $\alpha = 0$ , the gray area is smoother than that of (a). (c) gives the best result. (d) shows a mass of flecks. (e) Increasing the value of  $\alpha$  gives high kernel similarity, reflecting that the event-regularized prior precisely describes motion patterns.

generally reflects more accurate deblurring. When  $\beta$  is fixed, increasing the value of  $\alpha$  yields gradually steady performance, whereas the cases of  $\beta$  exhibit an almost opposite tendency. Visual and quantitative assessments show that the proposed event prior supplies a precise description of the shapes, structures and positions of moving objects in a latent sharp image and thus dominates rough deblurred results, and the  $L_0$  constraint works on auxiliary calibrations.

#### H. Analysis of Event Denoising Strength

In Equation (25), we exploit a calibration factor  $\omega$  to manage the level of denoising. Figure 9 studies its impact on denoised results. Setting a large value of  $\omega$  suppresses sparse events and retains only the most active (densest) ones, showing that increasing its value is equivalent to enhancing denoising strength by raising the filter threshold. In other words, valuable information might be lost although sufficient denoising can be obtained. The optimum  $\omega$  depends on cases and seeks a trade-off — a detector on autonomous vehicles might require a low value of  $\omega$  such that avoiding discarding the events triggered

TABLE III  
DETAILS OF OUR REAL NEUROMORPHIC DATASET.

Sample	Setting	Result
keyboard	camera shaking	uniform blurry images; events with noise
toy	camera shaking	uniform blurry images; events with noise
text_cambridge	camera shaking	uniform blurry images; events with noise
cathedral	camera shaking; weak illumination	uniform blurry images; events with increased noise
box	camera shaking; strong illumination	overexposed, uniform blurry images; events with noise
text_number1	moving object; weak illumination	underexposed, uniform blurry images; events with increased noise
text_number2	moving object; strong illumination	overexposed, uniform blurry images; events with noise
book	moving object	non-uniform blurry images; events with noise
text_intro	moving object	non-uniform blurry images; events with noise
badminton1	moving object	non-uniform blurry images; events with noise
badminton2	moving object; strong illumination	overexposed, non-uniform blurry images; events with noise
resolution_fast	moving object	uniform blurry images; events with noise
resolution_slow	moving object	uniform blurry images; decreased events

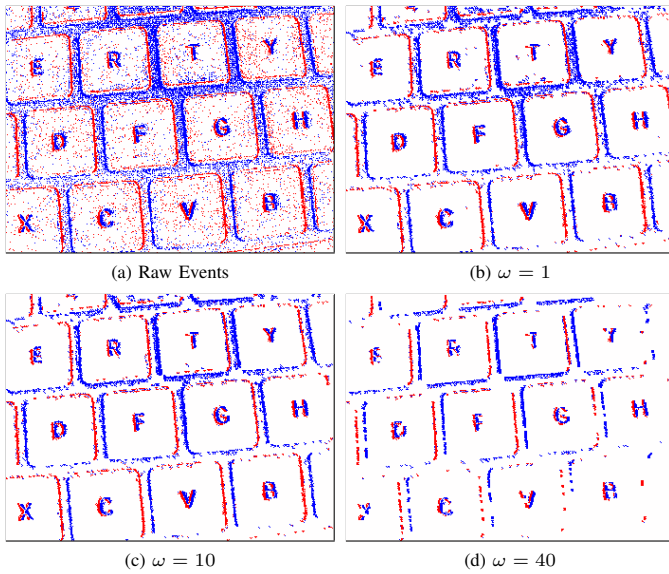


Fig. 9. Influences of the calibration factor  $\omega$  on denoised events.

by small obstacles, whereas a data collector in optical systems might prefer a high value for capturing noise-robust data.

## V. CONCLUSION

When capturing dynamic scenes, neuromorphic cameras output blurry images and noisy events due to the nature of the sensors. In this work, we bridge the two data sources to reconstruct blur-free images and noise-robust events. Our simple yet effective solution shows more satisfactory results compared with other methods and manifests greater robustness to several challenging cases (*e.g.*, extreme illumination and complicated motion patterns), paving the way for accurate high-level neuromorphic analysis. Nevertheless, since it relies on event information, we fail to faithfully recover a sharp image whose details are missing from the blurry one and are not recorded by the events. We discuss the limitation of our work in Appendix D and require further research to solve the challenging issue.

## APPENDIX A BLURRY IMAGES AND NOISY EVENTS DATASET

The motivation of this data collection work lies in that there is a lack of neuromorphic datasets for pairs of blurry images and noisy events in the community. Table III provides more details about each sample. For different samples, the count of events ranges from  $3 \times 10^5$  EPS (events per second) to  $8 \times 10^6$  EPS, and the images are recorded at a frame rate from 1 FPS (frames per second) to 25 FPS.

## APPENDIX B EXTENSION TO NON-UNIFORM DEBLURRING

We extend uniform deblurring to handle non-uniform motion blur, where a blurry image is split into multiple patches associated with different blur kernels. As such, a non-uniform blurry image  $\mathbf{B}$  can be modelled as

$$\mathbf{B} = \sum_{i=1}^{\infty} \mathbf{B}_i = \sum_{i=1}^{\infty} \mathbf{S}_i * \mathbf{k}_i, \quad (28)$$

where the  $i$ th patch  $\mathbf{S}_i$  of an image  $\mathbf{S}$  is blurred by the corresponding kernel  $\mathbf{k}_i$  to obtain the blurry patch  $\mathbf{B}_i$ . We can thus use our uniform deblurring to sharpen blurry patches and then acquire a complete sharp image by

$$\mathbf{S} = \sum_{i=1}^{\infty} \mathbf{S}_i. \quad (29)$$

Since our algorithm incorporates event information, and events only record the foreground with significant motion, we explore the use of uniform deblurring for non-uniform blurry images, as shown in Figure 10. The image-based competitor fails to deblur the image by uniform deblurring, since it has multiple conflicting kernels and cannot choose the correct one to estimate the sharp image. It then brings visible improvements by patch-by-patch processing. By contrast, our method achieves comparable results by the two treatments, although there are slight blur artifacts in the static background of our uniformly deblurred image. The study proves that event-based solutions have more precise positioning of the dynamic foreground and better robustness for different kinds of motion patterns.

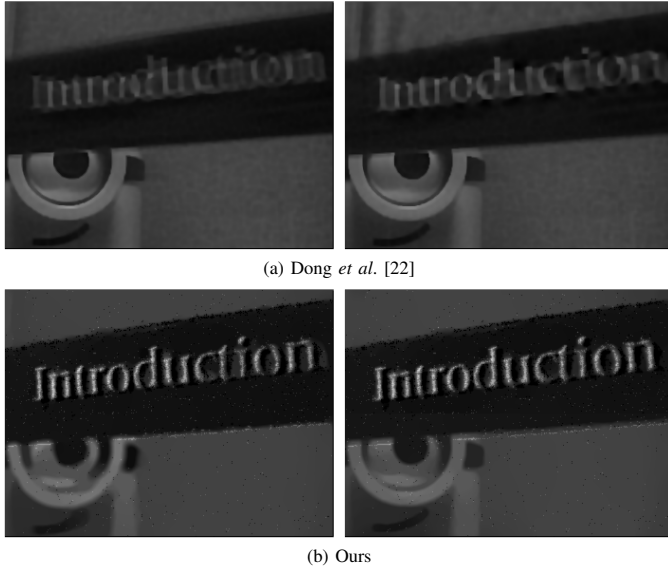


Fig. 10. Visual comparisons on deblurring the image with non-uniform blur by processing the image at once (left) or patch-by-patch (right). The examined algorithms keep the same configurations for the two cases.

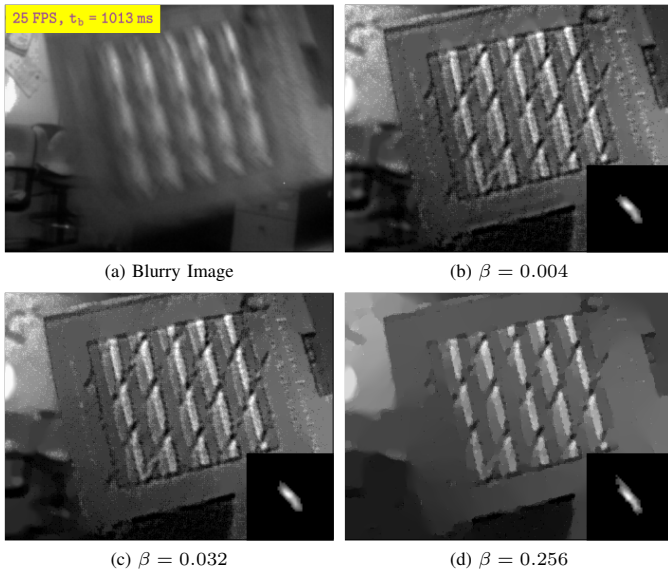


Fig. 11. Influences of  $\beta$  (when  $\alpha = 0.8$ ) on image deblurring.

#### APPENDIX C

##### ANALYSIS OF THE $L_0$ REGULARIZER FOR DEBLURRING

In Figure 11, we supply more information about how the  $L_0$  regularization affects deblurred images. When  $\beta = 0.004$  and the event-based constraint still dominates, we have a clear, sharp result that also contains observable artifacts (*i.e.*, white flecks). The artifacts are then suppressed as the  $L_0$  term prevails with a high value of  $\beta = 0.256$ , but the texture and structure details recorded in the events are also smoothed and erased, and the associated blur kernel is distorted.

#### APPENDIX D

##### LIMITATION DISCUSSIONS

Although our solution achieves outstanding results in evaluations, its limitation should also be of concern. Since the

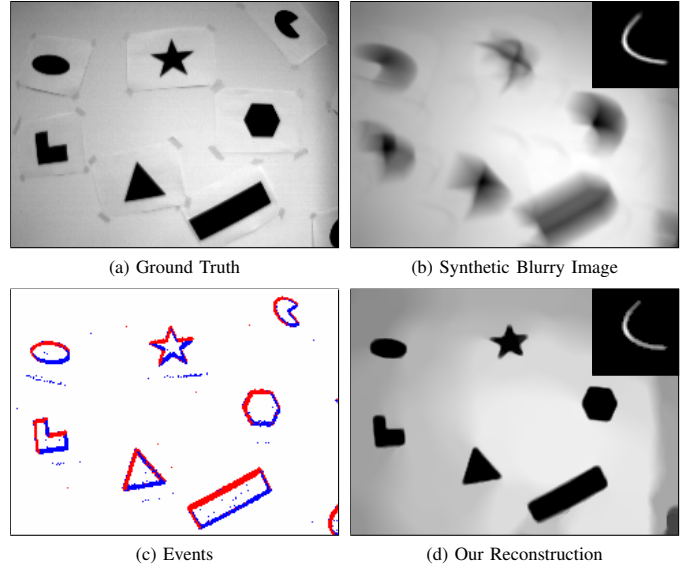


Fig. 12. A case where our method loses information during image deblurring.

proposed deblurring mechanism hinges on event priors, it cannot recover the details that are missing from both the blurry image and events, as the sample [40] given in Figure 12. A synthetic kernel blurs the ground truth to make the thin lines around the black shapes disappear. Even if the blur kernel can be faithfully estimated, our reconstruction still loses the thin lines since there are almost no events triggered by them.

#### REFERENCES

- [1] G. Gallego, T. Delbruck, G. M. Orchard, C. Bartolozzi, B. Taba, A. Censi, S. Leutenegger, A. Davison, J. Conradt, K. Daniilidis, and D. Scaramuzza, "Event-based vision: A survey," *IEEE Transactions on Pattern Analysis and Machine Intelligence*, vol. 44, no. 1, pp. 154–180, January 2022.
- [2] G. Taverni, D. P. Moeys, C. Li, C. Cavaco, V. Motsnyi, D. S. S. Bello, and T. Delbruck, "Front and back illuminated dynamic and active pixel vision sensors comparison," *IEEE Transactions on Circuits and Systems II: Express Briefs*, vol. 65, no. 5, pp. 677–681, May 2018.
- [3] A. I. Maqueda, A. Loquercio, G. Gallego, N. García, and D. Scaramuzza, "Event-based vision meets deep learning on steering prediction for self-driving cars," in *Proceedings of the IEEE/CVF Conference on Computer Vision and Pattern Recognition*, June 2018, pp. 5419–5427.
- [4] Z. Ge, P. Zhang, Y. Gao, H. K.-H. So, and E. Y. Lam, "Lens-free motion analysis via neuromorphic laser speckle imaging," *Optics Express*, vol. 30, no. 2, pp. 2206–2218, January 2022.
- [5] J. Li, J. Li, L. Zhu, X. Xiang, T. Huang, and Y. Tian, "Asynchronous spatio-temporal memory network for continuous event-based object detection," *IEEE Transactions on Image Processing*, vol. 31, pp. 2975–2987, April 2022.
- [6] S. Guo and T. Delbruck, "Low cost and latency event camera background activity denoising," *IEEE Transactions on Pattern Analysis and Machine Intelligence*, vol. 45, no. 1, pp. 785–795, January 2023.
- [7] P. Lichtsteiner, C. Posch, and T. Delbruck, "A  $128 \times 128$  120 dB 15  $\mu$ s latency asynchronous temporal contrast vision sensor," *IEEE Journal of Solid-State Circuits*, vol. 43, no. 2, pp. 566–576, February 2008.
- [8] C. Scheerlinck, N. Barnes, and R. Mahony, "Continuous-time intensity estimation using event cameras," in *Asian Conference on Computer Vision*, December 2018, pp. 308–324.
- [9] L. Pan, R. Hartley, C. Scheerlinck, M. Liu, X. Yu, and Y. Dai, "High frame rate video reconstruction based on an event camera," *IEEE Transactions on Pattern Analysis and Machine Intelligence*, vol. 44, no. 5, pp. 2519–2533, May 2022.

- [10] Z. Wang, Y. Ng, C. Scheerlinck, and R. Mahony, "An asynchronous kalman filter for hybrid event cameras," in *Proceedings of the IEEE/CVF International Conference on Computer Vision*, October 2021, pp. 448–457.
- [11] X. Zhang and L. Yu, "Unifying motion deblurring and frame interpolation with events," in *Proceedings of the IEEE/CVF Conference on Computer Vision and Pattern Recognition*, June 2022, pp. 17765–17774.
- [12] Z. W. Wang, P. Duan, O. Cossairt, A. Katsaggelos, T. Huang, and B. Shi, "Joint filtering of intensity images and neuromorphic events for high-resolution noise-robust imaging," in *Proceedings of the IEEE/CVF Conference on Computer Vision and Pattern Recognition*, June 2020, pp. 1609–1619.
- [13] H. Rebecq, T. Horstschaefer, and D. Scaramuzza, "Real-time visual-inertial odometry for event cameras using keyframe-based nonlinear optimization," in *British Machine Vision Conference*, September 2017.
- [14] Y. Li, H. Zhou, B. Yang, Y. Zhang, Z. Cui, H. Bao, and G. Zhang, "Graph-based asynchronous event processing for rapid object recognition," in *Proceedings of the IEEE/CVF International Conference on Computer Vision*, October 2021, pp. 934–943.
- [15] S. Shiba, Y. Aoki, and G. Gallego, "Secrets of event-based optical flow," in *European Conference on Computer Vision*, October 2022, pp. 628–645.
- [16] Z. Jia, K. You, W. He, Y. Tian, Y. Feng, Y. Wang, X. Jia, Y. Lou, J. Zhang, G. Li *et al.*, "Event-based semantic segmentation with posterior attention," *IEEE Transactions on Image Processing*, vol. 32, pp. 1829–1842, March 2023.
- [17] Z. Ge, H. Wei, F. Xu, Y. Gao, Z. Chu, H. K.-H. So, and E. Y. Lam, "Millisecond autofocus microscopy using neuromorphic event sensing," *Optics and Lasers in Engineering*, vol. 160, pp. 107247(1–9), January 2023.
- [18] Y. Hu, S.-C. Liu, and T. Delbruck, "v2e: From video frames to realistic DVS events," in *Proceedings of the IEEE/CVF Conference on Computer Vision and Pattern Recognition*, June 2021, pp. 1312–1321.
- [19] M. Gehrig, W. Aarents, D. Gehrig, and D. Scaramuzza, "DSEC: A stereo event camera dataset for driving scenarios," *IEEE Robotics and Automation Letters*, vol. 6, no. 3, pp. 4947–4954, July 2021.
- [20] L. Song, Z. Ge, and E. Y. Lam, "Dual alternating direction method of multipliers for inverse imaging," *IEEE Transactions on Image Processing*, vol. 31, pp. 3295–3308, April 2022.
- [21] J. Pan, Z. Hu, Z. Su, and M.-H. Yang, " $l_0$ -regularized intensity and gradient prior for deblurring text images and beyond," *IEEE Transactions on Pattern Analysis and Machine Intelligence*, vol. 39, no. 2, pp. 342–355, February 2017.
- [22] J. Dong, J. Pan, Z. Su, and M.-H. Yang, "Blind image deblurring with outlier handling," in *Proceedings of the IEEE/CVF International Conference on Computer Vision*, October 2017, pp. 2478–2486.
- [23] L. Pan, R. Hartley, M. Liu, and Y. Dai, "Phase-only image based kernel estimation for single image blind deblurring," in *Proceedings of the IEEE/CVF Conference on Computer Vision and Pattern Recognition*, June 2019, pp. 6034–6043.
- [24] D. Li, Y. Zhang, K. C. Cheung, X. Wang, H. Qin, and H. Li, "Learning degradation representations for image deblurring," in *European Conference on Computer Vision*, October 2022, pp. 736–753.
- [25] L. Pan, C. Scheerlinck, X. Yu, R. Hartley, M. Liu, and Y. Dai, "Bringing a blurry frame alive at high frame-rate with an event camera," in *Proceedings of the IEEE/CVF Conference on Computer Vision and Pattern Recognition*, June 2019, pp. 6820–6829.
- [26] H. Rebecq, R. Ranftl, V. Koltun, and D. Scaramuzza, "High speed and high dynamic range video with an event camera," *IEEE Transactions on Pattern Analysis and Machine Intelligence*, vol. 43, no. 6, pp. 1964–1980, June 2021.
- [27] P. Zhang, Z. Ge, L. Song, and E. Y. Lam, "Neuromorphic imaging with density-based spatiotemporal denoising," *IEEE Transactions on Computational Imaging*, vol. 9, pp. 530–541, May 2023.
- [28] T. Delbruck, "Frame-free dynamic digital vision," in *Proceedings of International Symposium on Secure-Life Electronics, Advanced Electronics for Quality Life and Society*, March 2008, pp. 21–26.
- [29] A. Khodamoradi and R. Kastner, " $O(n)$ -space spatiotemporal filter for reducing noise in neuromorphic vision sensors," *IEEE Transactions on Emerging Topics in Computing*, vol. 9, no. 1, pp. 15–23, January 2018.
- [30] Y. Feng, H. Lv, H. Liu, Y. Zhang, Y. Xiao, and C. Han, "Event density based denoising method for dynamic vision sensor," *Applied Sciences*, vol. 10, no. 6, p. 2024, March 2020.
- [31] J. Wu, C. Ma, L. Li, W. Dong, and G. Shi, "Probabilistic undirected graph based denoising method for dynamic vision sensor," *IEEE Transactions on Multimedia*, vol. 23, pp. 1148–1159, May 2020.
- [32] R. Baldwin, M. Almatrafi, V. Asari, and K. Hirakawa, "Event probability mask (EPM) and event denoising convolutional neural network (EDnCNN) for neuromorphic cameras," in *Proceedings of the IEEE/CVF Conference on Computer Vision and Pattern Recognition*, June 2020, pp. 1701–1710.
- [33] P. Duan, Z. W. Wang, X. Zhou, Y. Ma, and B. Shi, "EventZoom: Learning to denoise and super resolve neuromorphic events," in *Proceedings of the IEEE/CVF Conference on Computer Vision and Pattern Recognition*, June 2021, pp. 12824–12833.
- [34] G. Gallego, C. Forster, E. Mueggler, and D. Scaramuzza, "Event-based camera pose tracking using a generative event model," *arXiv preprint arXiv:1510.01972*, 2015.
- [35] L. Xu, C. Lu, Y. Xu, and J. Jia, "Image smoothing via  $l_0$  gradient minimization," *ACM Transactions on Graphics*, vol. 30, no. 6, pp. 1–12, December 2011.
- [36] L. Xu, S. Zheng, and J. Jia, "Unnatural  $l_0$  sparse representation for natural image deblurring," in *Proceedings of the IEEE/CVF Conference on Computer Vision and Pattern Recognition*, June 2013, pp. 1107–1114.
- [37] L. Chen, F. Fang, T. Wang, and G. Zhang, "Blind image deblurring with local maximum gradient prior," in *Proceedings of the IEEE/CVF Conference on Computer Vision and Pattern Recognition*, June 2019, pp. 1742–1750.
- [38] Y. Bai, G. Cheung, X. Liu, and W. Gao, "Graph-based blind image deblurring from a single photograph," *IEEE Transactions on Image Processing*, vol. 28, no. 3, pp. 1404–1418, March 2018.
- [39] H. Rebecq, R. Ranftl, V. Koltun, and D. Scaramuzza, "Events-to-video: Bringing modern computer vision to event cameras," in *Proceedings of the IEEE/CVF Conference on Computer Vision and Pattern Recognition*, June 2019, pp. 3857–3866.
- [40] E. Mueggler, H. Rebecq, G. Gallego, T. Delbruck, and D. Scaramuzza, "The event-camera dataset and simulator: Event-based data for pose estimation, visual odometry, and SLAM," *The International Journal of Robotics Research*, vol. 36, no. 2, pp. 142–149, February 2017.
- [41] R. Zhang, P. Isola, A. A. Efros, E. Shechtman, and O. Wang, "The unreasonable effectiveness of deep features as a perceptual metric," in *Proceedings of the IEEE/CVF Conference on Computer Vision and Pattern Recognition*, June 2018, pp. 586–595.
- [42] D. Czech and G. Orchard, "Evaluating noise filtering for event-based asynchronous change detection image sensors," in *IEEE International Conference on Biomedical Robotics and Biomechatronics*, June 2016, pp. 19–24.